Journal of the Korea Concrete Institute
Vol.17 No.6, pp.1053~1064, December, 2005

Cohesive Interface Model on Concrete Materials

In-Kyu Rhee[1)*] and Young-Sook Roh[2)]

[1)] *Track & Civil Engineering Dept., Korea Railroad Research Institute, Uiwang,437-757 Korea*
[2)] *Dept. of Architectural Engineering, Seoul National University of Technology, Seou,l 139-743 Korea*

(Received Feburary 24, 2005, Accepted October 30, 2005)

ABSTRACT

The mechanical damage of concrete is normally attributed to the formation of microcracks and their propagation and coalescence into macroscopic cracks. This physical degradation is caused from progressive and hierarchical damage of the microstructure due to debonding and slip along bimaterial interfaces at the mesoscale. Their growth and coalescence leads to initiation of hairline discrete cracks at the mesoscale. Eventually, single or multiple major discrete cracks develop at the macroscale. In this paper, from this conceptual model of mechanical damage in concrete, the computational efforts were made in order to characterize physical cracks and how to quantify the damage of concrete materials within the laws of thermodynamics with the aid of interface element in traditional finite element methodology. One dimensional effective traction/jump constitutive interface law is introduced in order to accommodate the normal opening and tangential slips on the interfaces between different materials(adhesion) or similar materials(cohesion) in two and three dimensional problems. Mode I failure and mixed mode failure of various geometries and boundary conditions are discussed in the sense of crack propagation and their spent of fracture energy under monotonic displacement control.

***Keywords** : crack, constitutive model, interface element, cohesion, fracture energy*

1. Introduction

The response behavior of cohesive and frictional materials such as concrete in the nonlinear range, particularly close to peak load and in the post-peak region, is extremely complex and has been intensively investigated in the past decades. A great variety of models has been proposed which is of little surprise and reflects the difficulties encountered, when one attempts to describe the macroscopic as well as mesoscopic response behavior by phenomenological constitutive models[4)]. It reflects the uncertainties in the interpretation of apparent failure mechanism in laboratory experiments with respect to the governing failure mechanism and their significance. Macroscopic response phenomena such as brittle failure or ductile softening are generally attributed to microstructural processes which appears to be one of the most important issues in view of constitutive modeling of strain softening materials[5,12,25)]. In this paper, a simple one dimensional effective traction/jump relation will be used for assessing the damage of lumped line and surface interface elements which also can not be simpler than C^0 element type.

Since the pioneering work of Ngo and Scoldelis[13)] for finite element analysis of reinforced concrete structures, the discrete crack concept is widely considered for micro- and meso- and macro-scale analysis of multi-material structures with the aid of development of computer hardware and software system. Modeling of discontinuities embedded in a continuous system requires a finite element technology which simulates the material interface and contains realistic constitutive properties. It is nontrivial to explore the feasibility of modeling the microstructural processes and investigate their influence on macroscopic response phenomena emphasizing the composite character of concrete. To this end, although this objective demands the material and morphological heterogeneities of concrete such as multiple phase composites, one can consider that the concrete material is isotropic and statistically homogeneous for simplicity.

* *Corresponding author*
Email address: rheei@krri.re.kr

Therefore, the level of observation is restricted in purely *'cohesive'* behavior of concrete material and plain concrete structures.

2. Mechanical damage in concrete

2.1 Concrete cracking

At the atomic level of observation, there are two types of bonds: (1) primary bonds(strong bonds), (2) secondary bonds(weak bonds). Primary bonds are classified as metallic, covalent and ionic bonds. Like ceramic, concrete may be classified to exhibit ionic bonds at the microscopic level of observation. In order to look at the insight of this ionic bonds, Coloumb's law of repulsive and attractive forces between atoms may represent the damage initiation as (a) separation in the form of debonding, (b) slip of these atoms by means of changing their equilibrium distance r. In order to understand, let us recall the typical example of ionic bond. Fig. 1 shows the example of ionic bonds of NaCl, or table salt. Fig. 2(a) and 2(b) shows the bond energy diagram and their second derivatives relation(stress-strain relation), respectively.

Starting from the damage mechanism associated with bonding energy argument at the microscopic level, this stress-strain relationship in Fig. 2(b) will be adopted directly later on the interface constitutive law. Now let us move on our observation frame to macroscale concrete crack. The phenomenological concept of a crack in brittle materials can traced back to a paper by Griffith(1920). Until then there was no explanation available for the known large discrepancy between the theoretically predicted and real tensile strengths of hard brittle materials. Griffith was the first to show that the real tensile strength of brittle materials was significantly lower than their theoretically predicted strength because they contained microcracks, e.g. defects, pores, voids, dislocations, etc.

Cracks introduce high stress concentration near their tips in an elastic brittle material. This is best illustrated by considering a sheet made of an elastic brittle material, such as concrete (Fig. 3)

The adjacent regions near crack tips in Fig. 3 which exhibit huge stress concentrations are developed. Griffith

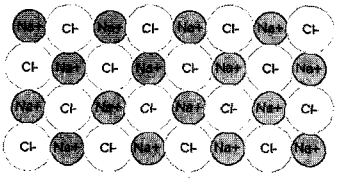

Fig. 1 Primary atomic bonds: Ionic bonds(NaCl)

(1920) already noted the inconsistency between the linear elastic fracture model and the real physical situation prevailing at the crack tip. The first attempt at including the cohesive forces in the crack tip region within the limit of elasticity theory was made by Barenblatt[1]. He assume that a large cohesive forces $\sigma(x)$ acts in a small zone of length d, so-called cohesive zone near the crack tip such that the crack opening displacement closes smoothly. The distribution of these cohesive forces is generally unknown. After this Barenblatt's idea, the first nonlinear theory of fracture mechanics for steel was proposed by Dugdale et al[3]. by defining the yield strength near crack tips. For concrete, Hillerborg[5] proposed the tension softening fracture process

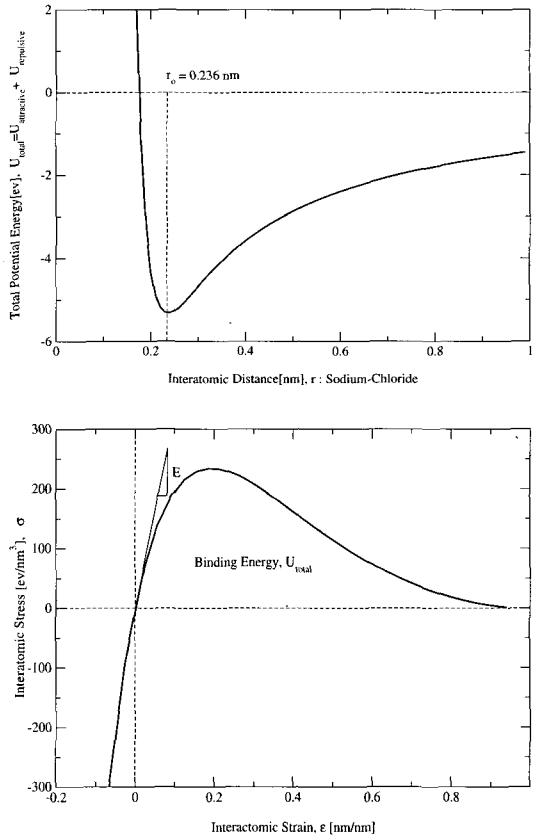

Fig. 2 Ionic bonds(NaCl) (a) bond energy diagram $U(r)$, (b) stress-strain diagram, $\sigma(r)$ and $\varepsilon(r)$

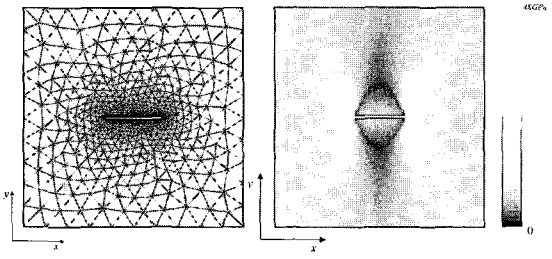

(a) Mesh layout, (b) Plot of major principal stress, σ_{pl}

Fig. 3 Uniform stretching test of slit-like flaw:

zone through a fictitious crack ahead of the pre-existing crack whose faces are acted upon by certain closing stresses such that there is no stress concentration at the tip of this extended crack(Figs. 4. and 5). It is immediately apparent that this condition is satisfied if faces of the crack close smoothly. The term '*fictitious*' is used to underline the fact that this closed crack cannot be continuous with full separation of its faces, as in a real traction-free crack.

2.2 Material laws for cohesive interfacial crack

A nominal traction field $\mathbf{t}$ (force/unit reference area) has both normal and shearing components in general. Two material points A and B, initially on opposite sides of the interfaces, are considered and the interfacial traction is taken to depend only on the displacement difference across the interface, $[|\mathbf{u}|]_{AB}$ in Fig. 6. At each point of the interface, the generalized traction $\mathbf{t}$ and the displacement jump $[|\mathbf{u}|]$ are defined as,

$$[|\mathbf{u}|] = \mathbf{R}\cdot[|\mathbf{u}|]_X \text{, where } \mathbf{R} = \text{Rotation matrix} \quad (1)$$

$$\mathbf{t} = \mathbf{R}^T\mathbf{t}_X \quad (2)$$

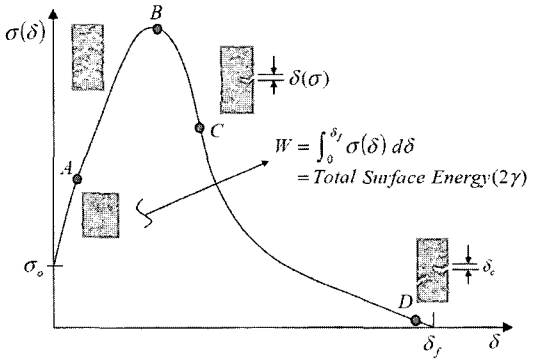

Fig. 4 Tension softening of concrete materials[25]

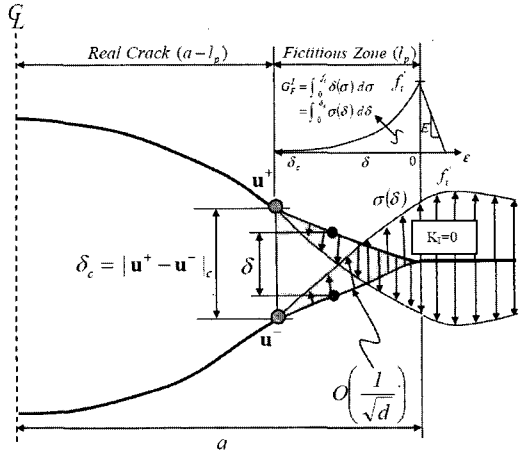

Fig. 5 Hillerborg's fictitious crack model[5]

The remaining task is how to characterize the traction-jump relationship in concrete materials. In the beginning of this chapter, the sodium-chloride(NaCl) example shows a exponential stress-strain relation in repulsion and quasi-linear in attraction as shown in Fig. 2(b). In order to upscale thi kind of interatomic relation the material point of concrete, the tension and compression behavior are described as the repulsion and attraction phenomenon. Needleman et al[12,28] proposed the hyperelasticity type of interface constitutive relation.

The existence of potential energy from the beginning and their first and second derivatives introduce the force-displacement and stress-strain relation respectively. However, in spite of convenience, this existence of potential shows that the work of separation is independent of the path or history that material point has experienced so far(Fig 7).

$$\phi = \phi([|\mathbf{u}|]) = -\int_0^{[|u|]} [t_n d[|u|]_n + t_t d[|u|]_t + t_s d[|u|]_s] \quad (3)$$

Camacho and Ortiz[2] suggested to consider the effective stress intensity factor for mixed-mode fracture (Margolin, 1984;Diens,1986), which leads to the fracture criteria,

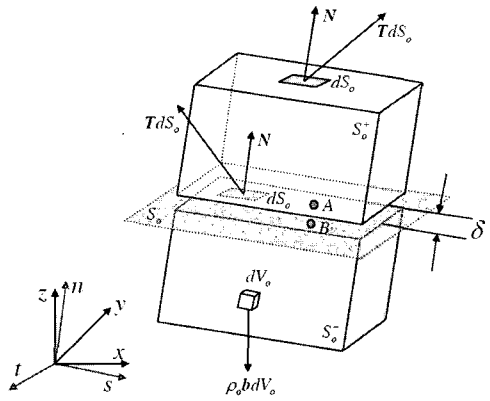

Fig. 6 Cohesive surface traversing a 3D body[18]

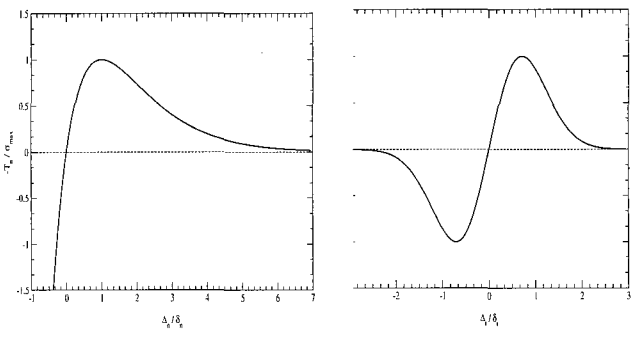

(a) Normal separation (b) Tangential slip law[8]

Fig. 7 Potential $\phi([|u|]_n, [|u|]_s)$:

$$\sigma_{eff} = \sqrt{\sigma^2 + \beta_\tau \tau^2} \le \sigma_{fr} \tag{4}$$

$$\sigma_{eff} = \sqrt{\beta_\tau \langle |\tau| - \mu |\sigma| \rangle} \le \sigma_{fr} \tag{5}$$

where β_τ is a shear stress factor, μ is the friction coefficent and σ_{fr} is a fracture stress. In order to estimate σ_{fr}, they assume that the fracture toughness K_{Ic} is a function with half-crack length a_o (Figs. 8 and 9).

Tvergaard and Hutchinson[23] have studied the role of plastic deformation in amplifying crack growth resistance in ductile failure using a cohesive zone model. They account for the interaction of the fracture process with the surrounding plastic zone by replacing the fracture process by a traction-separation relation applied to the plane of the crack which, in turn, is embedded within an elastic-plastic continuum(Fig. 10).

Since we are interested in damage measure at the material level in the spirit of damage mechanics such as Kachanov[8], The proposal of Camacho and Ortiz[2] looks simple and logical to characterize the concrete interface laws. Now we attempt to establish this idea with combination of material softening and damage measure for our own purpose.

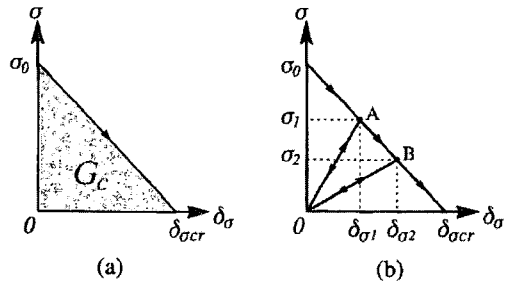

Fig. 8 Tensile cohesive relation by Camcho and Ortiz[2]

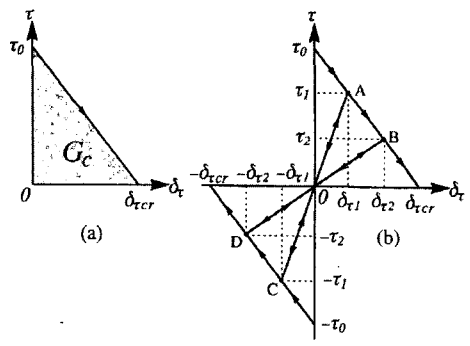

Fig. 9 Shear cohesive relation by Camacho and Ortiz[2]

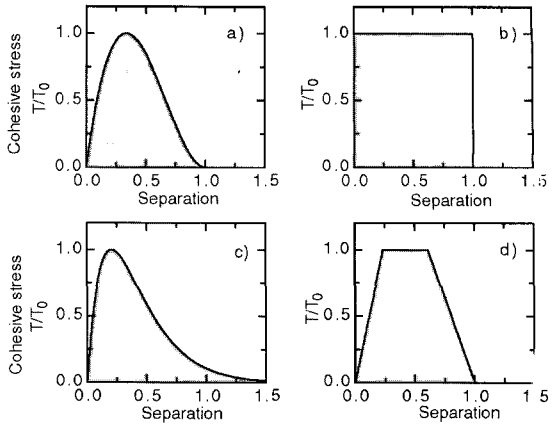

Fig. 10 Form of the traction-separation laws: (a) cubic, Needleman(1987), (b) constant, Schwalbe and Cornec(1994), (c) exponen tial, Needleman(1990), (d) trilinear, Tver gaad and Hutchinson(1992) by courtesy of Scheider(2001)

3. Cohesive interface model in concretes

3.1 Nodal constraints and interface element

Introducing multi-freedom constraints(MFCs) by changing the assembled master stiffness equations produce a modified system of equations. The modified system is he one submitted to the equation solver. Three methods or treating MFCs are (a) master-slave elimination, (b) penalty augmentation and (c) Largrangian multiplier adjunction. These nodal constraints in linear algebra are physically reflected by nature of *interface* element which will be used to model a potential cohesive interfacial crack. Naturally, penalty augmentation(similary with Largrangian multiplier approach) approach will discuss in the conjunction with interface formulation. In the presence of discontinuities the variational boundary problem to be solved is subjected to unilateral constraints. For instance, two bodies may only separate but must not interpenetrate each other along their common contact surface Γ_c,

$$\mathbf{g}_i^T \mathbf{u}_i \ge [|u|]_{oi}, \qquad \forall\, i \in \Gamma_c \tag{6}$$

where i is the number of nodes on Γ_c, $\mathbf{u}_i$ is the unknown displacement vector in Cartesian components, x, y and z, $\mathbf{g}_i$ is the connectivity vector between constrained degree of freedom, $[|u|]_{oi}$ is the amount of normal relative displacement representing full contact.

The conventional finite element methods approximate the potential energy Π_k through a kinematically ad-

missible displacement field, interpolated over the element domains from nodal displacement vectors. To minimize Π_k for the unknown state of the indeterminate boundary conditions, the functional needs be augmented either by Lagrangian multiplier or a surface energy term, growing the amount of constraint violation,

$$\Pi(\mathbf{u}) = \Pi_k(\mathbf{u}) + \frac{1}{2} w \sum_i (g_i^T u_i - [|u|]_{oi})^T (g_i^T u_i - [|u|]_{oi}) \rightarrow \min \tag{7}$$

Eq.(7) will be satisfied in a least-square sense by virtue of the quadratic form of additional term, representing the work done by 'push-back' forces $p_i(w)$, where $w >> 1$ regularizes the unilateral constraint problem,

$$\mathbf{p}_i(w) = w(\mathbf{g}_i^T \mathbf{u}_i - [|u|]_{oi}) \tag{8}$$

An algebraic equation system is obtained from first variation of the potential in Eq.(7), to which the constraint conditions are added in their 'perturbed' form,

$$\begin{bmatrix} \mathbf{K} & \mathbf{G} \\ \mathbf{G}^T & -\frac{1}{w}\mathbf{I} \end{bmatrix} \begin{Bmatrix} \mathbf{u} \\ \mathbf{p} \end{Bmatrix} = \begin{Bmatrix} \mathbf{f} \\ [|u|]_o \end{Bmatrix} \tag{9}$$

where $\mathbf{K}$ is the system stiffness matrix assembled from the individual elements, $\mathbf{f}$ is the given vector of the external nodal forces. The contact force $\mathbf{p}$ can be considered out owing to their proportionality to the amount of constraint violation.

$$\left\{ \begin{matrix} \mathbf{Ku} + \mathbf{Gp} = \mathbf{f} \\ \mathbf{G}^T\mathbf{u} - \frac{1}{w}\mathbf{Gp} = \mathbf{G}[|u|]_o \end{matrix} \right\} \Rightarrow [\mathbf{K} + w\mathbf{G}\mathbf{G}^T]\mathbf{u} = \mathbf{f} + w\mathbf{G}[|u|]_o \tag{10}$$

This penalty augmented system matrix is assembled in the usual direct stiffness procedure and the equation system of the same size as without constraints and is solved in conventional Newton-Rapson technique. Another important aspect is the selection of penalty parameter w. Clearly as $w \rightarrow \infty$, $\mathbf{K} + w\mathbf{G}\mathbf{G}^T$ become linearly dependent. Linear dependence means singularity. Hence $\mathbf{K} + w\mathbf{G}\mathbf{G}^T$ approaches singularity as $w \rightarrow \infty$. In fact, if w excced $1/\varepsilon_f = 10^{16}$ the computer will not be able to distinguish $\mathbf{K} + w\mathbf{G}\mathbf{G}^T$ from an exactly singular matrix. If $w << 10^{16}$ but $w >> 1$, the effect will be seen in increasing solution errors affecting the computed displacements $\hat{\mathbf{u}}$ returned by equation solver. These error, however, tends to be more of a random nature than the constraint violation error. Obviously we have two effects at odds with each other. Making w larger reduces the constraint violation error but increase the solution error. The best w is that which makes both errors roughly equal in absolute value. This tradeoff value is difficult to find aside from running numerical experiments. In the finite-precision arithmetic there exists thus an optimum choice of the penalty parameter w between constraint satisfaction and truncation error [16].

3.2 Finite element discretization

Neglecting body forces and inertia forces, the principle of virtual work equates the internal virtual work δW^{int} and the external virtual work δW^{ext} at the time t,

$$\delta \Pi = \delta W^{int} - \delta W^{ext} = \int_V \delta[|\mathbf{u}|]^T \mathbf{t}\, dV - \int_S \delta\mathbf{u}^T \mathbf{p}\, dS = 0 \tag{11}$$

where $\delta\mathbf{u}$ is the virtual displacement field and $\mathbf{p}$ is the applied interface loads and $\prod$ is the potential surface energy. Upon finite element discretization and approximation of the displacement field $\mathbf{u}$ through interpolation functions with

$$\mathbf{u} = \mathbf{N}\mathbf{u}^{el} \tag{12}$$

and,

$$[|\mathbf{u}|] = \mathbf{B}\mathbf{u}^{el} \tag{13}$$

we observe that Eq.(11) transforms into a set of algebraic equations,

$$\delta\mathbf{u}^T \int_V \mathbf{B}^T \mathbf{t}\, dV - \delta\mathbf{u}^T \int_S \mathbf{N}^T \mathbf{p}\, dS = 0 \tag{14}$$

which can be written as a residual force equation,

$$F(\mathbf{u}, \mathbf{p}) = F(\mathbf{t}) - F(\mathbf{p}) = 0 \tag{15}$$

where $F(\mathbf{t})$ is the internal force vector assembled from the element forces

$$F(\mathbf{t}) = \int_V \mathbf{B}^T \mathbf{t}\, dV \tag{16}$$

and $F(\mathbf{p})$ are the consistent nodal loads of the applied displacements or concentrated elemental forces. With the adoption of a constitutive relation,

$$\mathbf{t} = \mathbf{D}[|\mathbf{u}|] \tag{17}$$

the internal force vector takes the form

$$F(\mathbf{t}) = \int_V \mathbf{B}^T \mathbf{D}\mathbf{B}\, dV\, \mathbf{u} = \mathbf{K}\mathbf{u} \tag{18}$$

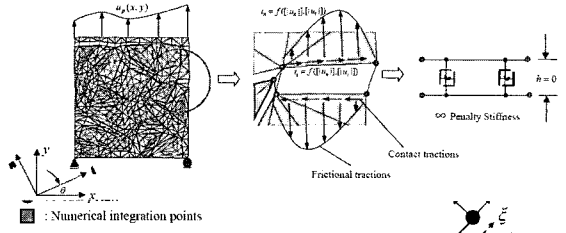

Fig. 11 General description for 2D interfaces

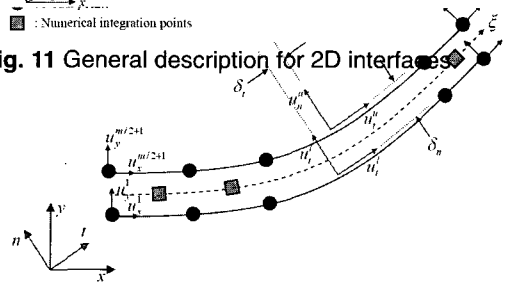

Fig. 12 Local and global coordinates system in general line interface element

In Eqs.(17) and (18), the stiffness is introduced in a rather generic manner. In a subsequent section, $\mathbf{D}$ is a nonlinear function of strains, i.e. $\mathbf{D}=\mathbf{D}([|\mathbf{u}|])$ and the tangent stiffness or some approximation thereof has to be used to solve Eq.(18).

3.3 2D Formulation

Consider an m-noded line interfaces as shown in Figs. 11 and 12. Each node has two translational degrees of freedoms, which leads to an element nodal displacement vector $\mathbf{u}^{el}$

$$\mathbf{u}^{el}=\left\{u_x^1,u_x^2,u_x^3,u_x^4,\cdots,u_y^{m-1},u_y^m\right\}^T \tag{19}$$

x, y denotes the Cartesian coordinates in global system. The continuous displacement field is denoted as

$$\mathbf{u}=\left\{u_t^l,u_n^l,u_t^u,u_n^u\right\}^T \tag{20}$$

where the superscript u and l indicates the upper and lower side of the interface respectively, and t and n denote the directions of tangential and normal to the interface line respectively. With an aid of the interpolation polynomials n, the relation between the continuous displacement field and the nodal displacement vector is derived as

$$\mathbf{u}=\mathbf{N}\mathbf{u}^{el} \tag{21}$$

in which $\mathbf{N}$ contains the interpolation polynomials according to

$$\mathbf{N}=\begin{bmatrix}\mathbf{n} & \mathbf{0}\\ \mathbf{0} & \mathbf{n}\end{bmatrix},\qquad \text{where } \mathbf{n}=\{N_1,N_2,\cdots,N_{m/2}\} \tag{22}$$

For the linear interpolation polynomial, e.g. two dimensional case: when $m=4$, $N_1=(1-\xi)/2$, $N_2=(1+\xi)/2$ while ξ is the isoparametric coordinate in the interface line. To relate the continuous displacement field to the relative displacements, a gradient matrix $\mathbf{G}$ is introduced.

$$\mathbf{G}=\begin{bmatrix}-1 & 1 & 0 & 0\\ 0 & 0 & -1 & 1\end{bmatrix} \tag{23}$$

when the relative displacement vector $[|\mathbf{u}|]$ is defined as $[|\mathbf{u}|]=\{[|u|]_x,[|u|]_y\}^T$, we obtain

$$[|\mathbf{u}|]=\mathbf{G}\mathbf{u} \tag{24}$$

Since we consider an element in which the global coordinate systems in the integration points coincide with the local coordinate system, no transformations are necessary. For an arbitrary oriented interface element, the product $\mathbf{GN}$ has to be transformed to the local tangential coordinate system of the integration point or node set by $\mathbf{R}$.

$$\begin{Bmatrix}[|u_t|]\\ [|u_n|]\end{Bmatrix}=\mathbf{R}\begin{Bmatrix}[|u_x|]\\ [|u_y|]\end{Bmatrix} \tag{25}$$

where $\mathbf{R}$ describes the rotation of $[|\mathbf{u}|]$ by

$$R=\frac{1}{J}\begin{bmatrix}\dfrac{\partial x}{\partial \xi} & \dfrac{\partial y}{\partial \xi}\\ -\dfrac{\partial y}{\partial \xi} & \dfrac{\partial x}{\partial \xi}\end{bmatrix},\quad J=\left[\left(\frac{\partial x}{\partial \xi}\right)^2+\left(\frac{\partial y}{\partial \xi}\right)^2\right]^{\frac{1}{2}} \tag{26}$$

The relation between nodal displacements and relative displacements for continuous elements is now derived from Eqs. (21),(24) and (26) as

$$\begin{Bmatrix}[|u_t|]\\ [|u_n|]\end{Bmatrix}=\mathbf{RGN}\mathbf{u}^{el}=\mathbf{B}\mathbf{u}^{el} \tag{27}$$

where relative displacement vs. nodal displacement matrix $\mathbf{B}$ reads

$$\mathbf{B}=\begin{bmatrix}\mathbf{-n} & \mathbf{-n} & \mathbf{0} & \mathbf{0}\\ \mathbf{0} & \mathbf{0} & \mathbf{n} & \mathbf{n}\end{bmatrix} \tag{28}$$

when the matrix $\mathbf{D}$ is used to denote the relation that describes the constitutive behaviors of the interface element

$$\mathbf{D}=\begin{bmatrix}d_{tt} & 0\\ 0 & d_{nn}\end{bmatrix} \tag{29}$$

Traction vs. relative displacement relation becomes

$$\mathbf{t}=\mathbf{D}[|\mathbf{u}|] \tag{30}$$

in which $\mathbf{t}=\{t_t,t_n\}^T$ represents the traction vector. The linear element stiffness $\mathbf{k}$ can now be obtained using the standard procedure of minimizing the total amount of potential energy. The amount of internal work done in the interface element equals

$$\delta U=\frac{1}{2}\int_A \delta[|\mathbf{u}|]\mathbf{t}dA \tag{31}$$

where $dA=hd\xi$ and h is the thickness of interfaces along the out of plane direction in 2D plane stress case. After invoking Eq. (31) results in

$$\delta U=\frac{1}{2}\delta\mathbf{u}^T\int_A \mathbf{B}^T\mathbf{D}\mathbf{B}dA\mathbf{u}=\frac{1}{2}\delta\mathbf{u}^T\mathbf{k}\mathbf{u} \tag{32}$$

The amount of external work is given by

$$\delta W=-\delta\mathbf{u}^T\mathbf{f} \tag{33}$$

with $\mathbf{f}$ the external consistent force vector. After variation of the total potential energy $\delta(U+W)=0$ with respect to the nodal displacement vector we obtain

$$\mathbf{k}\mathbf{u}=\mathbf{f} \tag{34}$$

where the stiffness k equals

$$\mathbf{k}=\int_A \mathbf{B}^T\mathbf{D}\mathbf{B}dA \tag{35}$$

For the numerically integrated interface elements, the integral in Eq.(35) is replaced by an integration over the tangential isoparametric coordinates ξ,

$$\mathbf{k}=h\int_{\xi=-1}^{\xi=+1}\mathbf{B}^T\mathbf{D}\mathbf{B}Jd\xi \tag{36}$$

Figs. 13 and 14 show that simple example of linear and quadratic 2D line interface element and their acting stretching eigenmodes.

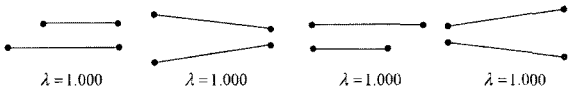

Fig. 13 Stretching eigenmodes in four node line interface element (Lobatto integration rule)

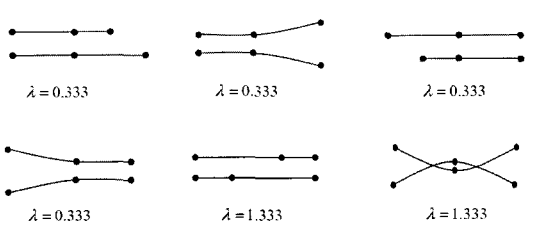

Fig. 14 Stretching eigenmodes in six node line interface element (Lobatto integration rule)

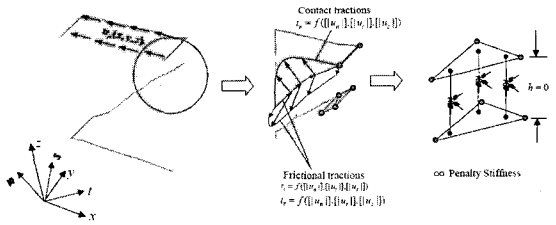

Fig. 15 General description for 3D interfaces

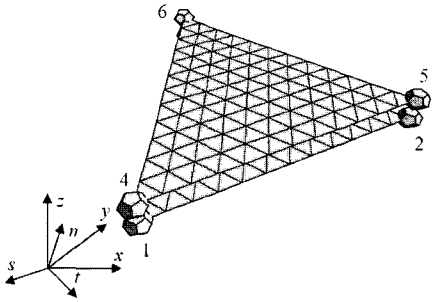

Fig. 16 A six node surface interface element

3.4 3 D Formulation

In a similar manner in 2D formulation, Figs. 15 and 16 depicts a surface interface element which connects two plane triangle elements. The coordinate x and the displacement field u which is continuous, on upper side u and lower side l are linearly interpolated using the shape functions N by

$$\mathbf{N}=\begin{bmatrix}\hat{\mathbf{N}} & \mathbf{0} & \mathbf{0}\\ \mathbf{0} & \hat{\mathbf{N}} & \mathbf{0}\\ \mathbf{0} & \mathbf{0} & \hat{\mathbf{N}}\end{bmatrix} \tag{37}$$

where

$$\mathbf{N}=\begin{bmatrix}N_1 & 0 & 0 & N_2 & 0 & 0 & N_3 & 0 & 0\\ 0 & N_1 & 0 & 0 & N_2 & 0 & 0 & N_3 & 0\\ 0 & 0 & N_1 & 0 & 0 & N_2 & 0 & 0 & N_3\end{bmatrix} \tag{38}$$

with

$$N_1=1-\xi-\eta,\quad N_2=\xi,\quad N_3=\eta \tag{39}$$

and ξ is the isoparametric coordinates of the interface element. The relative displacement field $[|u|]=u^u-u^l$ between side u and side l is obtained by defining Eq. (24).

The remaining work is to construct the rotational matrix in Eq.(27) with additional shear jump term in 3D. A local coordinate system is established at a point on the contact in Fig. 16 by first finding the vector normal to the contact surface. This is obtained as a cross-product of two vectors,

$$\mathbf{n}_p = \begin{Bmatrix} \frac{\partial x}{\partial \xi} \\ \frac{\partial y}{\partial \xi} \\ \frac{\partial z}{\partial \xi} \end{Bmatrix} \times \begin{Bmatrix} \frac{\partial x}{\partial \eta} \\ \frac{\partial y}{\partial \eta} \\ \frac{\partial z}{\partial \eta} \end{Bmatrix} \tag{40}$$

The unit vector in the direction normal to the surface is

$$\mathbf{n} = \frac{\mathbf{n}_p}{A} \tag{41}$$

where A is the length of $\mathbf{n}_p$ and represents the unit mapped area of the interface plane. The two tangent vectors are formed by

$$\mathbf{s} = \begin{Bmatrix} 1 \\ 0 \\ 0 \end{Bmatrix} \times \mathbf{n} \tag{42}$$

and

$$\mathbf{t} = \mathbf{s} \times \mathbf{n} \tag{43}$$

Now we are done for the transformation matrix **R** and ready to invoking this product **B** into general stiffness equation as in Eqs. (31) and (32). Figs. 17 and 18 show the selective stretching modes of linear and quadratic surface interfaces.

3.5 Damage in cohesive surfaces

Now we are attempting to insert the life of interface element itself. In order to do that, we discuss the earlier in section 2 regarding Camacho and Ortiz [2] model which well defined in terms of material softening as well as the material degradation due to progressive damage. Hence we adopt and alter some of details on the constitutive level however basic idea is similar since effective traction vs. jump relationship is a basic assumption.

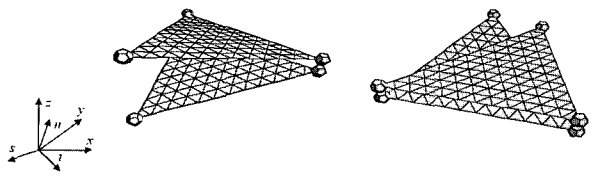

Fig. 17 Some stretching eigenmodes in 6 node surface interface element (Lobatto integration rule)

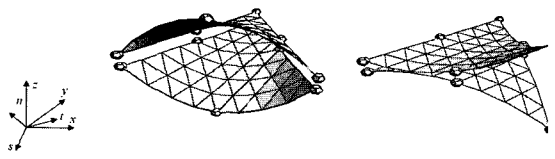

Fig. 18 Some stretching eigenmodes in 12 node surface interface element (Lobatto integration rule)

Traditional isotropic damage relation between the traction vector and the separation vector of a cohesive surface reads

$$\mathbf{t} = (1-\omega)[|\mathbf{u}|] \tag{44}$$

in which $\mathbf{t} = \{t_t, t_n\}^T$ and $[|\mathbf{u}|] = \{[|u_t|],[|u_n|]\}^T$ contain the normal and tangential components of the traction and separation to the cohesive surface, respectively. In continuum damage models, one generally assumes the damage variable ω to be a function of a history parameter κ, which is the function of some measure of the equivalent strain, ε^{eq}. Various definitions of the equivalent strain ε^{eq} have been proposed of which we mentioned the definition given by Mazar(1989) and Tijssens[21], in which only the positive, principle strains are used

$$\varepsilon^{eq} = \sqrt{\sum_{i=1}^{3} \langle \varepsilon_i \rangle^2} \tag{45}$$

where $\langle \bullet \rangle$ denotes the Macauley brakets. Motivated by the relative simplicity of Mazar's criterion and following Camacho and Ortiz[2], we let ω be a function of the equivalent one-dimensional cohesive separation ζ defined by

$$\zeta^2 = \langle [|u_n|] \rangle^2 + \alpha [|u_t|]^2 \tag{46}$$

in which the influence of the tangential slip $[|u_t|]$ can be varied through the normal separation parameter. The rate equations for the cohesive surface are now obtained as

$$\dot{\mathbf{t}} = (1-\omega)\mathbf{D}[|\dot{\mathbf{u}}|] - \dot{\omega}\mathbf{D}[|\mathbf{u}|] \tag{47}$$

in which $\dot{\omega}$ is obtained through

$$\dot{\omega} = \frac{d\omega}{d\zeta}\left[\frac{\partial \zeta}{\partial [|u_n|]}[|\dot{u}_n|] + \frac{\partial \zeta}{\partial [|u_t|]}[|\dot{u}_t|]\right] \tag{48}$$

Substitution of Eq. (48) into (47) results in the rate constitutive equations for the cohesive surfaces

$$\begin{bmatrix} \dot{t}_t \\ \dot{t}_n \end{bmatrix} = \begin{bmatrix} (1-\omega)d_o - \frac{d\omega}{d\zeta}\frac{d\zeta}{d[|u_t|]} d_o[|u_t|] & -\frac{d\omega}{d\zeta}\frac{d\zeta}{d[|u_n|]} d_o[|u_t|] \\ -\frac{d\omega}{d\zeta}\frac{d\zeta}{d[|u_t|]} d_o[|u_n|] & (1-\omega)d_o - \frac{d\omega}{d\zeta}\frac{d\zeta}{d[|u_n|]} d_o[|u_n|] \end{bmatrix} \begin{bmatrix} [|u_t|] \\ [|u_n|] \end{bmatrix} \tag{49}$$

The term $d\omega/d\zeta$ is defined through the 1D scalar relation

$$\sigma(\zeta) = (1-\omega(\zeta))d_o\zeta \tag{50}$$

in which σ and ζ are the one-dimensional traction and separation of the cohesive surface. Hence

$$\frac{d\omega}{d\zeta}=\frac{1}{d_o\zeta}\left[\frac{\sigma(\zeta)}{\zeta}-\frac{d\sigma(\zeta)}{d\zeta}\right] \qquad (51)$$

Here we limit ourselves to damage initiation and growth under tensile stresses. Initially the cohesive surface constitutive response is assumed to be elastic according to $\sigma(\zeta)=d_o\zeta$ where we take $d_o=\sigma_{\max}/[|u|]_1$ with $\sigma_{\max}$ the maximum tensile strength of the cohesive surface and $[|u|]_1$ the value of the equivalent cohesive separation ζ for which damage initiates. For separation $\zeta>[|u|]_1$ we assume softening of the cohesive response. Common approaches to define softening after peak load are linear or exponential softening laws. These will be adopted here according to

$$\sigma(\zeta)=\sigma_{\max}e^{\beta\left(1-\frac{[|u|]}{[|u|]_1}\right)}, \quad \zeta\geq[|u|]_1 \qquad (53)$$

For exponential softening, the rate of softening is determined by the separation parameter $[|u|]_2$. The localization of deformation and thus the prediction of the final fracture path is to a large extent determined by the initial softening slope of the cohesive law. For this reason, the value of β in the exponential softening is taken as $[|u|]_1/([|u|]_2-[|u|]_1)$ which results in equal initial softening behavior for linear and exponential softening. The softening response is illustrated in Fig. 19.

Figs. 20, 21 show the relationship of the normal traction and corresponding relative displacement in tension in terms of G_f^{Ia}. In order to avoid to interpenetration in compression, only tangential slip term is active in progressive damage. The role of the coupling factor α for shear contribution of mixed mode damage is shown in Figs. 20, 21. Normally, α range is from 0 to 1. The factor $\alpha=0$ means the material law only involves tensile action which is fully decoupled from the shear contribution and vice versa. When α is equal to 1, a full interaction between normal and tangential damage is considered.

Expanding to 3D effective damage model is pretty direction may be taken into account for evaluating effective traction/jump condition(Eq.54).

$$\zeta^2=\langle[|u_n|]\rangle^2+\alpha\left([|u_t|]^2+[|u_s|]^2\right) \qquad (54)$$

In order to implement 2D and 3D interface elements and their material nonlinearity to finite element method, a sophisticate finite element simulation platform FEM-C++[30] will be used for the main analyses. Full Newton-Rapson iterative methods are being used for the nonlinear analysis.

4. Benchmark tests for plain concretes

4.1 L-Shaped panel in 2D

The L-shaped plain concrete panel has become a popular benchmark test by B. Winkler, G. Niederwanger and Hofstetter[29] for the validation of computational models for numerical simulation of cracking of plain concrete. Hence, in order to provide experimental data, test on L-shaped structural members were performed. Test set-up with the geometric properties and the boundary conditions is shown in Fig. 22.

and

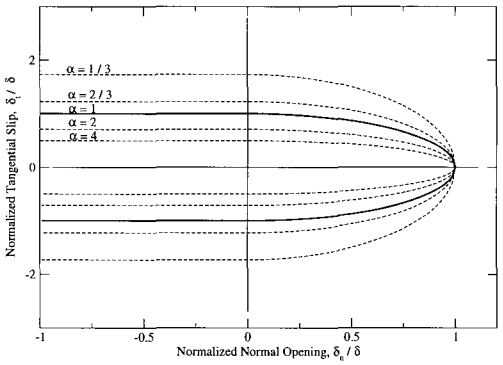

Fig. 20 Interaction between normal and tangential jump in 2D

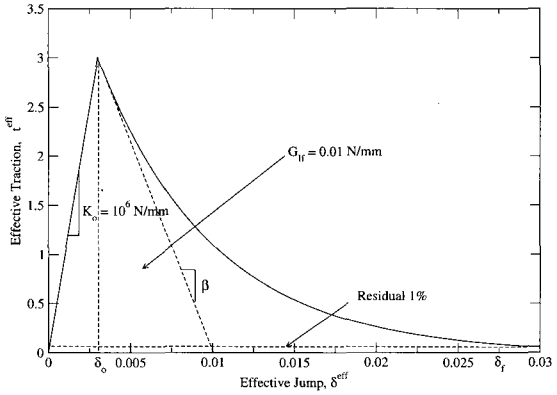

Fig. 19 One-dimensional material softening law

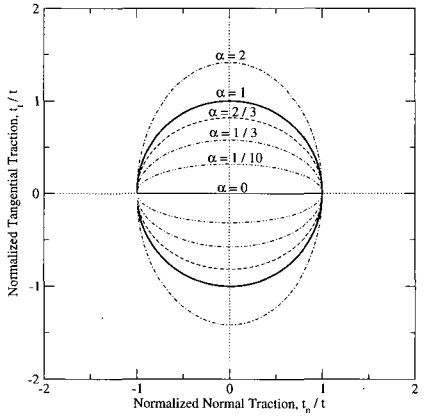

Fig. 21 Interaction between normal and tangential traction in 2D

250*mm*, respectively and its thickness is 100*mm*. The lower horizontal edge of the vertical edge was fixed. A vertical line load, acting uniformly across the thickness opposite to the direction of gravity, was applied on the lower horizontal surface of the horizontal leg at a distance of 30mm from the vertical end face. Shortly before reaching the maximum load the experiment was switched from load-control to displacement control. The composition of the concrete is given in Table 1. The average values of the uniaxial material parameters for concrete and the standard deviations were determined on the basis of three samples for each test series summarized in Table 2. In addition to the axial tensile strength, the flexural tensile strength and the splitting tensile strength were specified. Poisson's ratio was stated to be $\nu = 0.18$.

The specific fracture energy G_f^I was determined by means of direct tensile tests. These tests resulted in a relatively large scatter of the specific fracture energy, ranging from 0.065 to 0.09 *N/mm*. Three tests on identical L-Panels were carried out. The displacements were measured at four different points by inductive pick-ups, denoted as WTK Nr. 1 to 4 in Fig. 23. The relationship between the load and the vertical displacement at the point of load application is shown in Fig. 23 as obtained from tests on three identical panels. In addition, the relationship between the load and the horizontal displacement of the corner formed by the long edges of the panel(measured by the inductive pick-up WTK Nr. 2) is shown in this figure.

Figs. 24 to 26 are shown in that the influence of the shear interaction ratio α is a critical factor for the secondary crack path. Initially a diagonal tension crack is developed due to the rotation of the upper panel part. This is a purely Mode I failure. All four different α cases show identical diagonal tension crack. After propagating further, the corner zone exhibits complex stress states which determine the secondary crack path(bifurcation point). When $\alpha = 0$, 1/3 and 2/3 the results show two different crack branches due to another tensile stress state. These numerical results are poor match with the experimental result also experiencing numerical difficulties after the bifurcation point. However, when $\alpha = 1$, the secondary crack path becomes unique and tends to propagate the diagonal cracks towards the opposite horizontal face. This is in good agreement with the actual crack pattern.

Table 1 Composition of the concrete

Composition	Specific gravity(kg/m^3)
Sand, 0-2 mm	1,316
Sand, 2-4 mm	470
Sand, 4-8 mm	94
Portland cement	340
Water	180

Table 2 Uniaxial material parameters for concrete

parameters	Mean value (N/mm^2)	Standard deviation
Cylindrical compressive strength	31.00	2.65
Axial tensile strength	2.70	0.19
Flexural tensile strength	6.39	0.52
Splitting tensile strength	2.66	0.05
Tangent modulus of elasticity	25850.00	1381.00

4.2 Uniaxial compression test in 3D

Normally, mode I test in most of cases provide relatively good results because of their simple opening mechanism

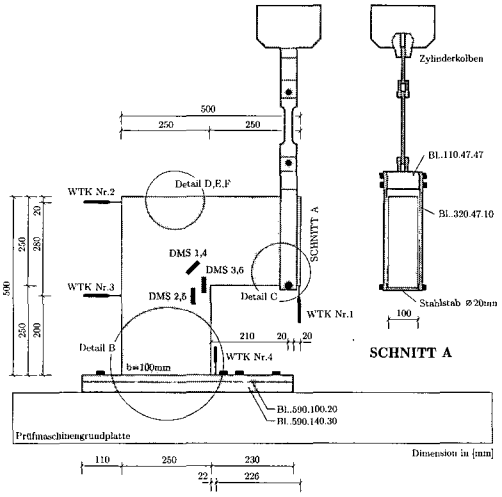

Fig. 22 Layout of L-shaped panel: test set-up

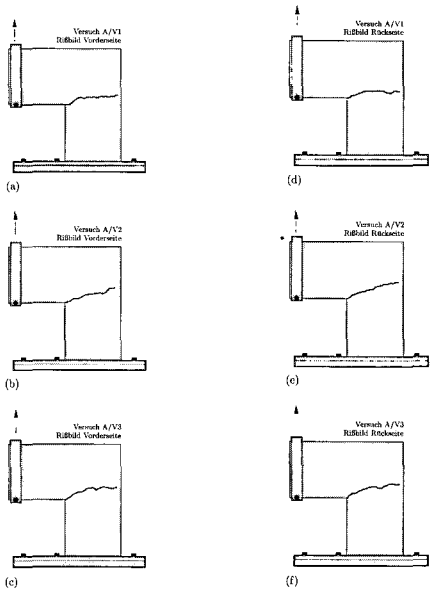

Fig. 23 Cracks at the front surface(left) and back face(right) before failure obtained from three tests on identical L-shaped panels

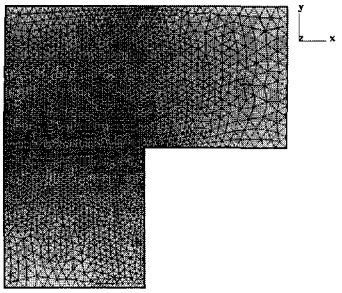

Fig. 24 2D FE unstructured mesh for L-shaped panel: 17343 nodes, 5781 for TRI2D, 8566 for INT2D

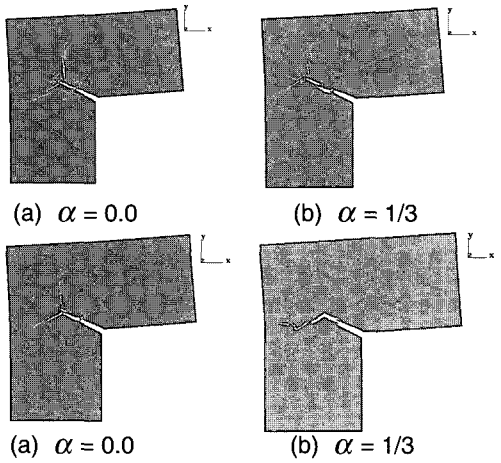

Fig. 25 Crack patterns obtained from FE analy sis with 2D fournode line interface element

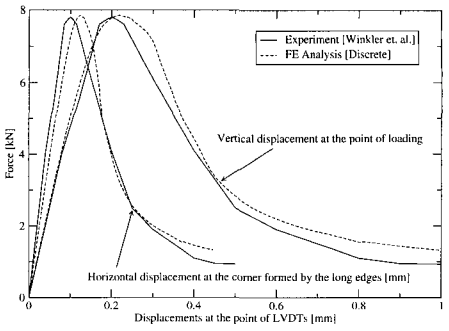

Fig. 26 Load-displacement diagram from three tests on identical L-shaped panels: (a) vertical displacement at the point of load application, (b) horizontal displacement at the corner formed by the long edges

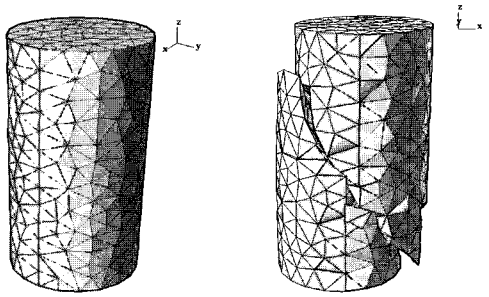

Fig. 27 Cylinder test: (a) geometry and basic mesh layout, (b) deformed mesh layout with 2D surface interfaces

besides of some subtle issues[31]. The failure mode of compression tests are more complex than the Mode I experiment. Now we are attempting to analyze the uniaxial compression test of standard concrete cylinder which is 150mm by 300mm. Since the effective damage assumption of the constitutive laws allow for slipping damage under compres-sion. It may not be close enough to realistic material behavior. Similarly to the above 2D case study, the shear interaction factor α is assumed to be equal and set to 0.8 for this uniaxial compression test.

A general description of the problem and the basic mesh layout are shown in Fig. 27. A total of 16,336 nodes (49,008 dofs) are being used to connect 11,920 elements (TETRA:4,084, INT3D:7,835). The material properties are E=20,000MPa, $\nu = 0.2$, $f_t^{'} = 3.0$MPa and $G_f^{IIa} = 1.2$ N/mm. The loading surfaces are only constrained axially so that the specimen is under uniaxially compression. The experiment of this cylinder test was performed by Roh and Xi(2000) with normal weighted concrete specimen. Fig. 27(b) shows the diagonal failure surface with an angle approximately 56°. Also Fig. 28 shows that the finite element analysis result shows failure earlier rather than the experimental one. The force-displacement plot gives an encouraging result but still a remaining question is the determination of shear interaction factor α. First, this cylindrical test specimen is axially symmetric so that one would easily choose α to behave isotropic sense. However, the determination of this factor is in fact depending upon the problem characteristics. This would be a main shortcoming of this material modeling assumption although it has interaction between normal and tangential components Thereby, adjacent continuum elements are not damaged in this approach. Using this technique, the behavior of the material is split into two parts, the damage-free continuum with elastic material behavior that can vary across the body, and the interspersed cohesive interface zones between continuum elements, which represent localized damage of material. In discrete crack model, 'potential' cracks are spread over the FE mesh domain with zero-thickness interface elements that initially nearly enforce continuity of tractions and displacements across the elements boundaries. They are subjected to a mixed mode failure criterion. Once the failure criterion is satisfied, 'potential' crack candidates can open or slide following the governing softening law. Two and three dimensional material model in line or surface interfaces are discussed and corresponding two benchmark tests are analyzed and discussed with experimental evidences. Although the material model introduced here is not completely satisfied with generalized problem with different geometries and boundary layer effect, this paper provides the practical crack analysis approach in the sense of strong discontinuity of materials and structures.

Acknowledgements

The lead author wishes to acknowledge support by the Smart Infra-Structure Technology Center (SISTeC) under grants of KOSEF and the second author is supported by the Infra-Structures Assessment Research Center (Project No.C104A1020001) under grants of Korean Ministry of Construction and Transportation (MOCT).

References

1. G. I., Barenblatt, "The formation of equilibrium cracks during brittle fracture: General ideas and hypotheses-axially symmetric cracks," *Journal of Applied Mathematics and Mechanics*, vol.23, 1959.
2. G. Camacho and M. Ortiz, "Computational modeling of impact damage in brittle materials," *International Journal of Solids and Structures*, Vol.33, 1996, pp.2899~2938.
3. D.S. Dugdale., "Yielding of steel sheets containing slits," *Journal of the Mechanics and Physics of Solids*, Vol.8, 1960.
4. M. Elices, G.V. Guinea, J. Gomez and J. Planas, "The cohesive zone model: advantages, limitation and challenges," *Engineering Fracture Mechanics*, Vol.69, 2002, pp.137~163.
5. A. Hillerborg, M. Modeer, and P.E. Petersson, "Analysis of crack formation and crack growth in concrete by means of fracture mechanics and finite elements," *Cements and Concrete Research*, Vol.6, 1976, pp.773~782.
6. J.-M. Honberg, *Concrete joints*, Mechanics of Geomaterial Interfaces, A.P.S. Selvadurai and M.J. Boulon(Eds), 1995.
7. B. Karihaloo, *Fracture mechanics and structural concrete*, Concrete Design and Construction Series, UK, 1994.
8. M. Kachanov, "Effective elastic properties of cracked solids: Critical review of some basic concepts," *Appl. Mech.* Rev., Vol. 45, No.8, 1992, pp.304~335.
9. D. Kincaid and W. Cheney., Numerical analysis: *Mathematics of scientific computing*, Brooks/Cole, New York, 2002, pp.1~788.
10. H.R. Lotfi and P.B. Shing, "Interface model applied to fracture of masonary structures," *Journal of Structural Engineering*, Vol.120, 1994, pp.62~80.
11. J.G.M. van Mier and M.R.A. van Vliet, "Uniaxial tension test for the determination of fracture parameters of concrete: State-of-the-Arts," Engineering Fracture Mechanics, Vol.69, 2000, pp.235~247.
12. A. Needleman, "A continuum model for void nucleation by inclusion debonding," *Journal of Applied Mechanics*, No.54, 1987, pp.525~531.
13. D. Ngo and A.C. Scordelis, "Finite element analysis of reinforced concrete beams," *ACI journal*, 1967, pp.152~163.
14. J. Planas, M. Elices, G.V. Guinea, F.J. Gomez, D.A. Cendon and I. Arbilla, "Generalizations and specializations of cohesive crack models," *Engineering Fracture Mechanics*, Vol.70, 2003, pp.1759~1776.
15. A. Griffith, "Theory of rupture," In Proc. 1st Int. Congress on Appl. Mech., Delft, The Netherlands, 1924, pp.55~63.
16. I. Rhee and W. Kim, "Analysis of shear behavior of lightweight reinforced concrete beam using interface elements," *Journal of Korean Society of Civil Engineers*, In press, 2006.
17. I. Rhee, H.U. Lee, J.S. Lee, and W. Kim, "Failure analysis of reinforced concrete bridge column using interface elements," *1st International Conference on Advanced Nondestructive Evaluation, Jeju International Conference Center, Korea* , Nov. 7th-9th 2005, 136pp.
18. G. Ruiz, A. Pandolfi and M. Ortiz, "Three dimensional cohesive modeling of dynamics mixed mode fracture," *International Journal for Numerical Methods in Engineering*, Vol.52., No.1-2, 2001, pp.97~120.
19. I. Scheider, *Cohesive model for crack propagation analyses of structures with elastic-plastic material behaviors*, GKSS Research Center, Geesthacht, WMS 2001, pp.1~41.
20. J.C.J. Schellekens and R. de Borst, "On the numerical integration of interface elements," *International Journal for Numerical Methods in Engineering*, Vol.36, No.7, 1993, pp.43~66.
21. M.G.A. Tijssens, *On the cohesive surface methodology for fracture of brittle heterogeneous solids*, Ph.D. thesis, Technische Universiteit Delft, 2001, pp.1~110.
22. T. Stankowski, *Numerical simulation of progressive failure in particle composites*, Ph.D. thesis, University of Colorado at Boulder, 1990, pp.1~118.
23. V. Tvergaard, "Cohesive zone representations of failure between elastic or rigid solids and ductile solids," *Engineering Fracture Mechanics*, Vol.70, 2003, pp.1859-1868.
24. K. Willam, I. Rhee, and Y. Xi, "Thermal Degradation of Heterogeneous Concrete Materials," *Journal of Materials in Civil Engineering*, ASCE, Vol.17, 2005, pp.276~285.
25. K. Willam, I. Rheem, and B. Shing, "Interface damage model for thermomechanical degradation of heterogeneous materials," *Computer Methods in Applied Mechanics and Engineering*, Vol.193, 2004, pp.3327~3350.
26. K. Willam, T. Stankowski, K. Runesson, and S. Sture, "Simulation issues of distributed and localized failure computations," *Proceedings on Cracking and Damage-Strain Localization and Size Effects, Mazars, J. and Bazant, Z. Eds.*, Elsevier Applied Sciences, London and New York, 1990, pp.363~378.
27. K. Willam, "Constitutive models for engineering materials," *Encyclopedia of Physical Science and Technology, Third Edition*, Vol.3, Academic Press, 2002, pp.603~633
28. X-P. Xu and A. Needleman, "Numerical simulations of fast crack growth in brittle solids", *Journal of Mechanics and Physics for Solids*, Vol.42, No.9, 1994, pp.1397~1434.
29. NW-IALAD, *Tg2: Continuum based material problems for dam concrete*, European Research Network, 2004, website:http://nw-ialad.uibk.ac.at/Wp2/
30. Department of Aerospace Engineering and Science, *FEM-C++: A totally objected oriented program for finite element modeling*, University of Colorado at Boulder, 2004, pp.1~200.
31. K. Duan, X.Z. Hu and F.H. Wittmann, "Boundary effect on specific fracture energy of concrete", *Fracture Mechanics of Concrete Structures*, Vol. 1, Conference Proceedings of FRAMCOS-5, Vail CO, USA 2004, pp.205~212.